One-step synthesis, characterization, and visible light photocatalytic activity of pure and Zn-doped SnO₂ nanoparticles

D. Madhan[1] · P. Rajkumar[2] · P. Rajeshwaran[3] · A. Sivarajan[4] · M. Sangeetha[5]

Abstract A one-step microwave irradiation route was used to synthesize undoped and Zn-doped SnO_2 nanoparticles for the first time. The morphologies, structures and optical properties of the as-prepared samples were characterized by X-ray powder diffraction, field emission scanning electron microscopy (FESEM), energy-dispersive X-ray spectroscopy, UV–Vis spectra and photoluminescence spectra analysis. The results clearly revealed that both the pure and doped samples had a tetragonal rutile-type structure and a space group of P42/mnm have formed directly during the microwave irradiation process. FESEM studies illustrate that both the pristine and Zn-doped SnO_2 form in spherical-shaped morphology with an average diameter around 41–32 nm, which is in good agreement with the average crystallite sizes calculated by Scherrer's formula. Optical studies reveal that both pristine and Zn-doped SnO_2 direct transitions occur with the bandgap energies in the range of 3.43–3.26 eV. The photocatalytic activities of the pure and Zn-doped SnO_2 samples were evaluated by the degradation of methylene blue rhodamine B in an aqueous solution under visible light irradiation. The photocatalytic activity and reusability of Zn (10 wt%)-doped SnO_2 was much higher than that of the pure SnO_2. The improvement mechanism by zinc doping was also discussed.

1 Introduction

The degradation of organic pollutants in water and air by photocatalysis, using semiconductors, has attracted extensive attention during recent 20 years [1]. Semiconductor photocatalysts have been widely investigated in the field of photochemistry and environmental protection, such as the photocatalytic degradation of environmental pollutants using near-UV or solar light. Among various kinds of metal oxide semiconductors, SnO_2 semiconductors have been keenly studied due to their excellent chemical stability and optical and electrical properties [2]. SnO_2 has the rutile-type tetragonal structure belonging to the P42/mnm space group. The lattice parameters are $a = b = 4.7382$ Å and $c = 3.1871$ Å, and the bandgap energy is in the ultraviolet range between 3.5 and 3.8 eV as estimated from experimental results and theoretical calculations [3]. Its high optical transparency, electrical conductivity, and chemical stability make it a very attractive material for solar cells, heat mirrors, catalysis, and gas sensing applications [4].

Up to now, a variety of methods have been used to synthesize of SnO_2 in powder or thin film form: co-precipitation [5], sol–gel method [6], spray pyrolysis [7], and hydrothermal technique [8]. Among these techniques, microwave irradiation is particularly attractive due to its operation simplicity, low cost, high purity, homogeneous distribution of doping element, less time consuming (about 10 min), and for large-scale production [2].

✉ D. Madhan
madhand14@yahoo.com

1 Department of Physics, KSR Polytechnic College, Tiruchengode 637 215, Tamilnadu, India

2 Department of Physics, TRP Engineering College, Trichy 621 105, Tamilnadu, India

3 Department of Chemistry, King College of Technology, Namakkal 637020, Tamilnadu, India

4 Department of Chemistry, Government Arts College, Thiruverumbur 620022, Tamilnadu, India

5 Department of Chemistry, KSR College of Technology, Tiruchengode 637 215, Tamilnadu, India

Chemical doping is a suitable method to enhance the photocatalytic properties of nanocrystalline SnO_2. Recently many metallic elements such as Ni [9], Cr [10], Zn [11], and Sb [12] have been proved to the effective dopants in improving the photocatalytic properties of SnO_2. Among these materials, Zn-doped SnO_2 attracts much interest in particular due to the photocatalyst performance of SnO_2 by modifying the structure, size, or morphology through different synthesis routes such as microwave, hydrothermal, hydrolysis method, and so on. So in the present investigation, we have synthesized pure and Zn-doped SnO_2 nanoparticles by a novel microwave irradiation method. To the best of our knowledge, this is the first preliminary report about structural, optical, and photocatalytic activity of pure and Zn-doped SnO_2 nanoparticles by microwave irradiation method. Moreover, the method is simple, cost-effective, and less time-consuming compared with other methods.

2 Experimental procedure

2.1 Synthesis of Zn-doped WO_3 nanoparticles

All chemicals used in this study were of analytical grade and were used without further purification. $SnCl_2 \cdot 2H_2O$ and $ZnCl_2 \cdot 2H_2O$ were used as tin and zinc sources, respectively. The starting solution was prepared by mixing of $SnCl_2 \cdot 2H_2O$ in deionized water to make 0.1 M solution. Appropriate amount of $ZnCl_2 \cdot 2H_2O$ in (0, 5 and 10 wt%) deionized water was added to the above solution. pH of the sol was adjusted to 8 with the addition of 2 ml of NH_4OH. The dropping rate must be well controlled for chemical homogeneity. After attaining the pH value, 5 ml of distilled water is added for quick response of microwave with precursor solution. The resulting precipitate was transferred into Teflon-lined household microwave oven (2.45 GHz) under optimum power of 360 W and irradiated for 15 min in air atmosphere. Pure SnO_2 nanopowders were prepared in a similar manner without the use of zinc source. The final product was in gray and pale white color for pure and Zn-doped SnO_2, respectively.

2.2 Characterization techniques

Pure and Zn-doped SnO_2 nanopowders were successfully characterized by the following techniques. The structure and crystallite size were analyzed by powder X-ray diffraction (XRD) using Bruker diffractometer within the 2θ range of 10°–80° using CuK_α as X-ray source ($k = 1.5406$ Å). The particle size and morphology were analyzed using field emission scanning electron microscopy (FESEM) and were recorded on (FEI—

QUANTA–FEG 250) analyzer. The optical transmittance of the nanopowders was recorded at room temperature by a Perkin Elmer UV/VIS/NIR Lambda 19 spectrophotometer in the wavelength range of 300–900 nm. Photoluminescence spectra of the samples were collected at room temperature by using Cary Eclipse (el02045776) fluorescence spectrophotometer in the wavelength range of 300–600 nm with a Xe laser as an exciting source and excitation wavelength of 325. The Fourier transform infrared spectra (FTIR) of the samples were collected using a 5DX FTIR spectrometer.

3 Results and discussion

3.1 XRD analysis

The phase formation and purity of the pure and Zn-doped SnO_2 nanoparticles were investigated by XRD as shown in Fig. 1. All the observed peaks can be indexed in agreement with the expected phase of SnO_2. All the diffraction peaks in the pattern correspond to the tetragonal rutile-type structure, which matched well with the standard JCPDS value (card no: 41-1445). For Zn-doped SnO_2 samples, no secondary phase (Zn or ZnO or, SnO) was observed, which indicates that the pure crystallinity and substitution of Zn into SnO_2 site. This suggests that Zn ions have substituted, at least partially, Sn in the SnO_2 matrix without changing the tetragonal structure. It was also noted that the small peak shift was observed for lower angle side for Zn-doped samples when increasing the Zn concentrations. Moreover, the intensity of the peak decreases with an increase in the zinc concentrations. These results clearly indicate that Zn^{2+} substituted in SnO_2 host lattice site. The lattice parameters
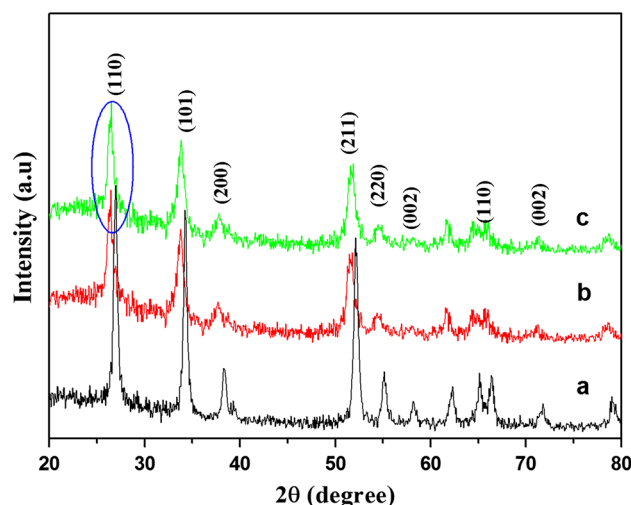

Fig. 1 Powder XRD pattern of SnO_2 nanoparticles **a** pure SnO_2 **b** 5 wt% Zn **c** 10 wt% Zn

Table 1 Lattice parameters and crystallite size of SnO$_2$ nanoparticles with different Zn concentrations

Zn concentrations (wt%)	Crystallite size (nm)	Lattice parameters		Cell volume
		a(Å)	b(Å)	(Å3)
0	41	4.7471	3.1925	71.94
5	37	4.7498	3.1938	72.05
10	32	4.7501	3.1941	72.11

of pure SnO$_2$ were estimated at $a = 4.7471$ (Å) and $c = 3.1925$ (Å). After zinc doping, these parameters slightly increase with increase in the zinc concentrations (Table 1). This phenomenon should be attributed to the similar ionic radii of Zn^{2+} ion (0.74 Å) with respect to the Sn^{4+} ion radius (0.69 Å).

The average crystalline sizes of the pure and Zn-doped SnO$_2$ nanoparticles were calculated by using Scherrer's equation [2].

$$d = \frac{K\lambda}{\beta \cos \theta}$$

where d is the mean crystallite size, K is the shape factor taken as 0.89, λ is the wavelength of the incident beam, β is

the full width at half maximum, and θ is the Bragg angle. The average crystalline size of pristine SnO$_2$ was found to be 41 nm, and it was further decreased to 32 nm for 10 wt% zinc-doped SnO$_2$. This result suggests that the grain growth is concealed due to doping of zinc into Sn site.

3.2 Field emission scanning electron microscopy analysis

Field emission scanning electron microscopy is a useful technique to determine the morphology and particle size of the nanoparticles. Figure 2 shows the field emission scanning electron micrographs of undoped and Zn (5 and 10 wt%)-doped SnO$_2$ nanoparticles. The images reveal that most of the particles have been formed as fine spheres in the all samples, although in the pure SnO$_2$ nanoparticles, several are elongated. Well-dispersed particles were observed for the Zn-doped samples. However, a small aggregation of particles has been observed in the pure SnO$_2$ samples as compared to Zn-doped samples. The average particle size was found to be 45, 42, and 34 nm for pure and Zn (5 and 10 wt%)-doped SnO$_2$, respectively. The calculated particle sizes are in good agreement with the

Fig. 2 FESEM image of SnO$_2$ nanoparticles **a** pure SnO$_2$ **b** 5 wt% Zn **c** 10 wt% Zn **d** EDS spectra of Zn (10 wt%)-doped SnO$_2$ nanoparticles
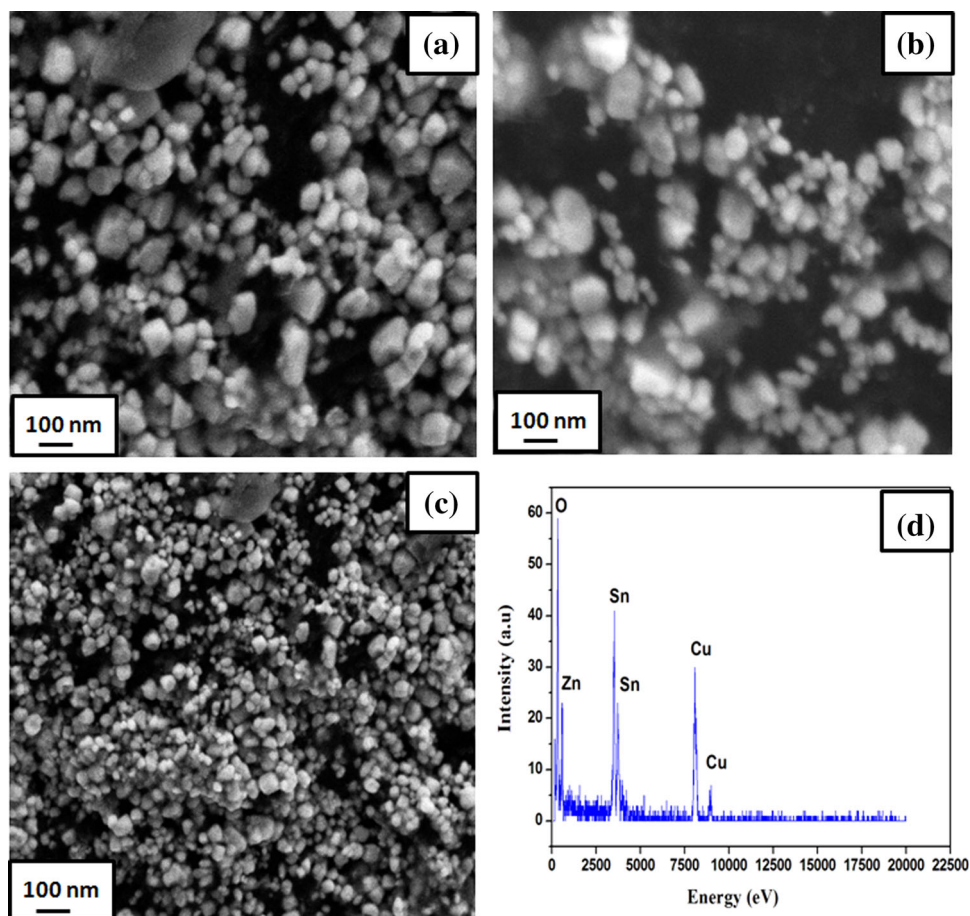
crystallite size estimated by XRD method. The surface composition of Zn (10 wt%)-doped SnO_2 can be determined by FESEM-based energy-dispersive spectroscopy (EDS) analysis as shown in Fig. 2d). The surface of the SnO_2 nanoparticles also exhibited elements of Sn, O, and Zn. The Cu element was found in the composition, due to the grid used to for EDS measurements. The calculated stoichiometry ratio from the EDS measurements was well matched with initial precursor which had been taken for synthesis process. The molar ratio of Sn/Zn is 10:1, which contains 9.8 wt% of Zn dopant.

3.3 UV–Vis transmission spectra analysis

In order to confirm the optical property such as transmission, absorptions, and substitution of Zn into SnO_2 site, the samples were characterized by UV–Vis transmission spectra analysis. Figure 3a shows the UV–Vis transmission spectra analysis of pure and Zn-doped SnO_2 samples. It is observed that the optical transparency of the pure SnO_2 decreases with the increase in the Zn content and the absorption edge between 300 and 370 nm, owing to the relatively large exciting binding energy. A considerable redshift is observed in the absorption edges with the increase in Zn content from 0 to 10 wt%, which indicates the decrease in band gap of SnO_2 on doping. The absorption coefficient (α) was calculated from the transmission spectra using equation [13],

$$\alpha = 1/t \ \ln(1/T)$$

where T is the optical transmission and t is the thickness of the samples. The band gap energy of the pure and Zn-doped SnO_2 samples was calculated from Fig. 3b using the formula [14],

$$\alpha h\nu = A(h\nu - E_g)^m$$

where α is the absorption coefficient, h is the Planck's constant, ν is the frequency of incident light, E_g is the energy band gap of material, and m is the factor governing the direct/indirect, etc., transition of electron from the valance band to the conduction band. The bandgap energy was calculated as 3.43, 3.31 and 3.26 eV for pure and Zn (5 and 10 wt%)-doped SnO_2 samples (Fig. 3b). The observed decrease in bandgap energy can be attributed to the sp–d exchange interactions between the band electrons and the localized d electrons of the Zn^{2+} ions substituting Sn^{4+} ions in semiconducting host lattice. Similar findings were observed in Cu-doped SnO_2 nanoparticles [15].

3.4 Photoluminescence spectra analysis

Photoluminescence characterization is another effective method to study the intrinsic nature of SnO_2, such as

oxygen vacancies and energy bands [16]. Figure 4 shows the PL emission spectra of both pure and Zn-doped SnO_2 samples measured from 300 to 600 nm using a 325-nm He–Cd laser. There are three emission peaks centered in all the samples at wavelengths of 426, 484, and 533 nm, respectively. The first two peaks centered in the blue emission region, 426 and 484 nm, with the corresponding energy of 2.87 and 2.63 eV, are clearly lower than the deduced band gap, and are attributed to the presence of oxygen vacancies on the surface. It was also noted that the Zn-doped samples show broad and increase the prominent emission peaks intensity more than the pure SnO_2 samples. In the pure SnO_2 host, the emission is attributed to electron transmission, mediated by defect levels in the band gap, such as oxygen vacancies, tin interstitials, and so forth. Certainly, after incorporating the Zn ions into the SnO_2 host matrix, the defect still plays a dominant role, with respect to the luminescence processes. In SnO_2, the oxygen vacancies are present in three different charge states: V_o^o, V_o^+, and V_o^{++}, in which V_o^o is a very shallow donor [17]. Among the different types of oxygen vacancies, the 533-nm peak related to single oxygen vacancies (V_o^+) [18].

3.5 Fourier transform infrared spectra analysis (FTIR)

Fourier transform infrared (FTIR) spectroscopy is a technique that provides information about the chemical bonding or molecular structure of materials. Figure 5 shows FTIR spectra of pure and Zn-doped SnO_2 (5 and 10 wt%) samples in room temperature. The absorption bands at $3461 \ cm^{-1}$ attributed to stretching vibration of surface hydroxyl group or adsorbed water, which is probably due to the fact that the spectrum was not recorded in situ, and some readsorption of water from the ambient atmosphere has occurred [16]. The bands appearing at $1625 \ cm^{-1}$ are related to the vibration of tin-hydroxyl (Sn–OH) bond [19]. The broad band at ~ 672 and 484^{-1} is associated with the O–Sn–O bridge functional groups of SnO_2, which confirms the presence of SnO_2 in the crystalline phase [19]. This is in good agreement with the results of the XRD analysis. After Zn doping, these peaks were shifted to lower wavenumbers and this may have been due to the decrease in size of the doped samples.

3.6 Photocatalytic activity setup

The photocatalytic activity setup was fabricated by Vadivel et al. [20]. The photocatalytic experiment on the prepared samples for the photodegradation of dyes is performed at ambient temperature. The photocatalytic activities of pure and Zn-doped SnO_2 samples were evaluated by the degradation of two types of dyes, including methylene blue
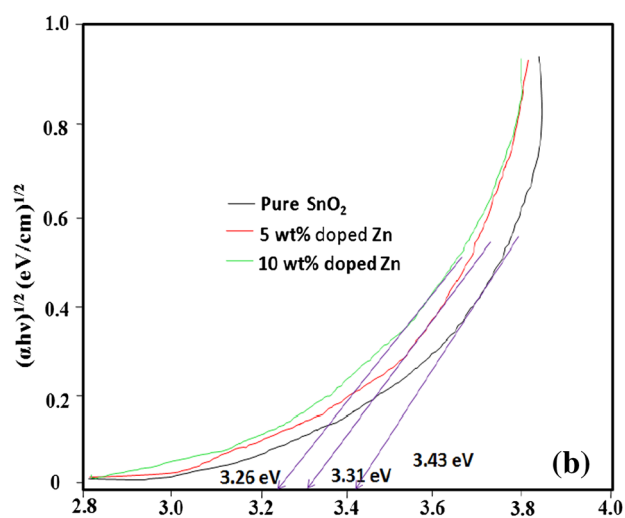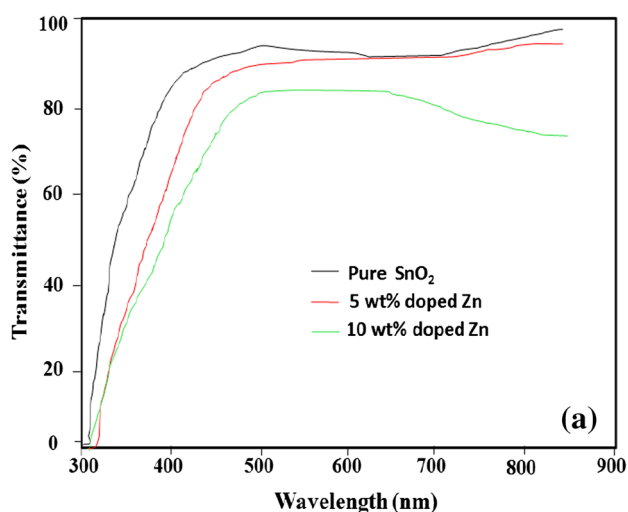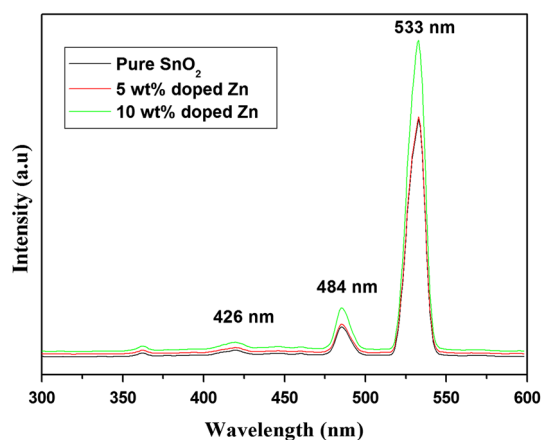
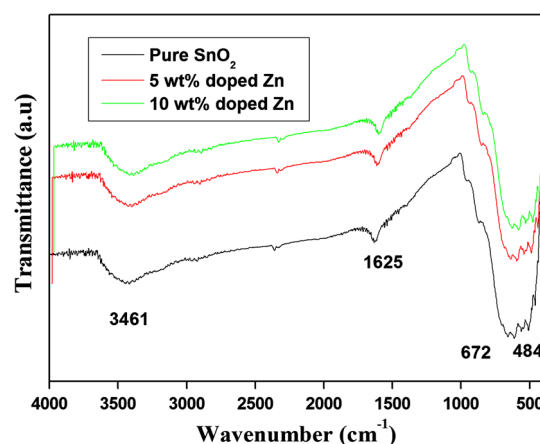**Fig. 5** FTIR spectra of SnO_2 nanoparticles with different Zn content

(MB) and rhodamine B (RHB) solution, in visible light irradiation. For the photocatalytic activity measurements, the dye solution prepared by adding a particular concentration (for example, 200 mL, $C_0 = 10$ mg L^{-1}) and particular amount of synthesized material was diluted into the dye solution. The 125-W high-pressure mercury lamp was used as a light source. The samples/dye solution was irradiated in the horizontal direction, and the distance between the UV lamp and the glass/dye solution was kept within 25 cm. Then, the solution has to be kept in the dark room and well stirred with the magnetic stirrer for more than 30 min to attain the equilibrium condition throughout the solution. The concentration of the aqueous suspensions (MB and RHB) in each sample was analyzed using UV–Vis spectrophotometer at a wavelength of 664 nm. The photocatalytic efficiency was calculated from the expression $\eta = (1 - C/C_0)$, where C_0 is the concentration of dyes (MB and RHB) before illumination and C is the concentration of dyes after a certain irradiation time.

3.6.1 Photocatalytic activity measurements

The photocatalytic activities of pure and Zn-doped SnO_2 samples were evaluated based on their ability to degrade various dyes (MB and RHB) under visible irradiation. The results showed that the time of the illumination and the quantity of the photocatalyst have obvious influence on the degradation of the reactive dyes. The photocatalytic evaluations of MB and RHB dye solution degradation are shown in Figs. 6 and 7. In Figs. 6 and 7, we have plotted the graph between degradation percentage of MB and RHB dyes concentration in the aqueous sample after UV illumination in the presence of a typical pure and Zn (5 and 10 wt%)-doped SnO_2 samples. The photocatalytic activity of Zn-doped samples increased with increasing Zn ion
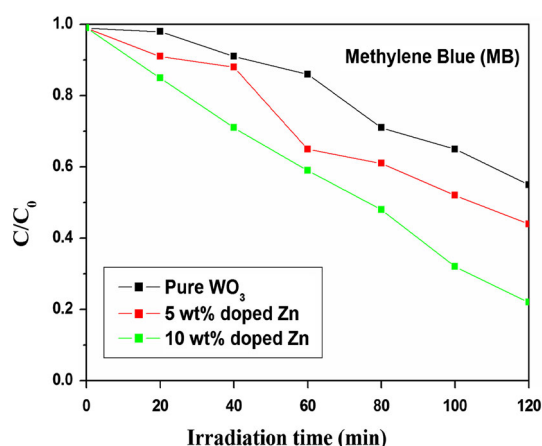

Fig. 3 UV–Vis spectra of SnO_2 nanoparticles with different Zn content **a** transmittance spectra **b** bandgap energy determination

Fig. 4 Photoluminescence spectra of SnO_2 nanoparticles with different Zn content

Fig. 6 Photocatalytic degradation of methylene blue (MB) using Zn–SnO$_2$ catalyst under visible light irradiation
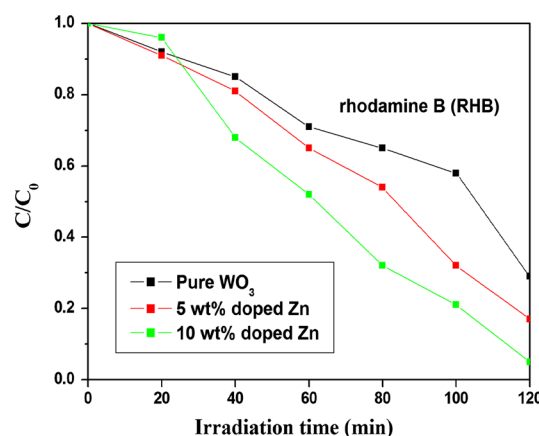

Fig. 7 Photocatalytic degradation of rhodamine B (RHB) using Zn–SnO$_2$ catalyst under visible light irradiation

concentrations. With the reaction time at 120 min, the MB degradation efficiencies of pure and Zn (5 and 10 wt%)-doped SnO$_2$ samples are about 45, 56, and 78 %, respectively. Similarly, the RHB degradation efficiencies of pure and Zn (5 and 10 wt%)-doped SnO$_2$ samples are about 71, 82, and 95 %, respectively. Thus, a threefold improvement in photocatalytic activity of RHB was observed when Zn (10 wt%)-doped SnO$_2$ samples were used upon 120 min UV light irradiation. The photocatalytic activity significantly improved due to Zn^{2+} doping showing highest photocatalytic activity of RHB decolorization (95 %). The reusability of the Zn (10 wt%)-doped SnO$_2$ samples as photocatalyst is also studied by collecting and reusing the same photocatalyst for multiple cycles. As shown in Fig. 8, after seven runs of photodegradation of RHB, the photocatalytic activity of the Zn–SnO$_2$ samples shows a slight degeneration due to incomplete recollection and loss during washing. Thus, the Zn–SnO$_2$ samples used as photocatalyst are quite stable and have massive potential application in water treatment. The photocatalytic properties of the catalyst strongly depend on their bandgap energy, morphology, particle size, and surface modification. These could be achieved through the Zn doping. The enhanced photocatalytic activity of Zn-doped samples due to decreasing the particle size and also bandgap energy of pristine SnO$_2$ could be attributed to the introduction of acceptance energy levels below the conduction band of SnO$_2$.

The photocatalytic mechanism of RHB by Zn-doped SnO$_2$ catalysts is shown in Fig. 9. For SnO$_2$ with the bandgap energy of 3.51 eV, theoretically, it can be excited by the photons with the wavelengths under 363 nm, but it shows only a modest photocatalytic activity under UV light in the present experimental conditions. This is probably due to the rapid recombination of the photogenerated
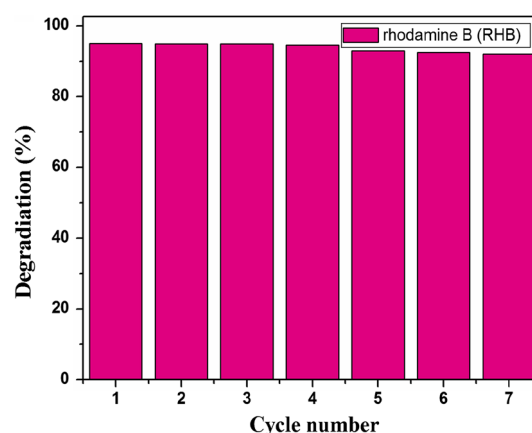

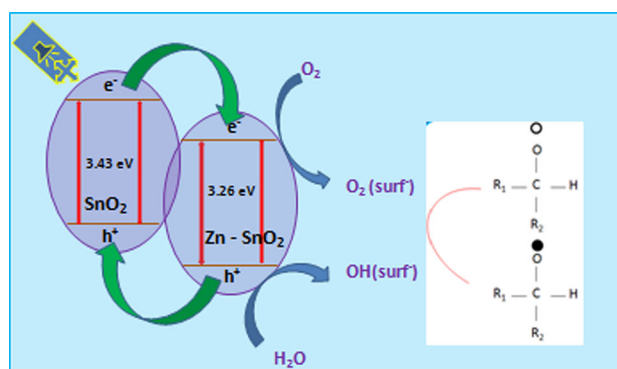**Fig. 8** Seven cycles of degradation of RHB using Zn–SnO$_2$ as the photocatalyst

Fig. 9 Schematic representation for photocatalytic mechanism of RHB in Zn–SnO$_2$ catalyst

electron–hole pairs in SnO$_2$. Zn-doped SnO$_2$ with the bandgap energy of 3.25 eV can be excited by the photons with the wavelengths under 384 nm. The CB of SnO$_2$ is

lower than that of Zn-doped SnO_2. Therefore, the past can act as a sink for the photogenerated electrons [21]. While the holes move in the opposite direction from the electrons, photogenerated holes might be intent within the Zn-doped SnO_2 particle, making charge separation more efficient, resulting in Zn-doped catalyst showing stronger photocatalytic activity [22]. At the same time, more RHB molecules are adsorbed on the surface of Zn–SnO_2 catalyst, enhancing the photoexcited electron to the conduction band and concurrently increasing the electron transfer to the adsorbed O_2. Furthermore, the smaller bandgap energy of Zn-doped SnO_2 may play a crucial role in enhancing the visible light photocatalytic activity of SnO_2 catalyst.

4 Conclusions

In summary, we have successfully prepared pure and Zn-doped SnO_2 nanoparticles by one-step microwave irradiation technique for the first time. Powder XRD results suggest that SnO_2 with tetragonal rutile-type crystal structure and the results are in good agreement with the standard JCPDS data (card no: 41-4115). Elongated spherical-shaped morphology with an average particle size around 45–34 nm was observed by FESEM. A considerable redshift in the absorption edge and decreasing the bandgap energy from 3.43 to 3.26 eV were observed by using UV–Vis spectra analysis. Moreover, UV and PL results suggested that photoabsorption of Zn-doped SnO_2 was extended to the visible light region. It was supposed that Zn dopant introduced new impurity levels between the conduction and valence band of SnO_2, leading to narrower band gap and enhancing the visible light absorption. The photocatalytic activity of pure and Zn-doped SnO_2 catalysts was determined by degradation of MB and RHB under visible light irradiation. Zn-doped catalysts show highest photocatalytic activity compared with pristine SnO_2. The recycling test demonstrates that degradation rate of Zn–SnO_2 catalyst is quite stable and as no decrease in the activity for the first four cycles. The result suggests that Zn-doped SnO_2 catalyst may have potential applications in pollutant removal as a highly efficient photocatalyst and also in waste water treatment.

References

1. W. Cun, Z. Jincai, W. Xinming, M. Bixian, S. Guoying, P. Ping'an, F. Jiamo, Appl. Catal. B: Environ. **39**, 269 (2002)
2. M. Parthibavarman, K. Vallalperuman, S. Sathishkumar, M. Durairaj, K. Thavamani, J. Mater. Sci. **25**, 730 (2014)
3. A. Bouaine, N. Brihi, J. Phys. Chem. C **111**, 2924 (2009)
4. M. Parthibavarman, B. Renganathan, D. Sastikumar, Curr. Appl. Phys. **13**, 1537 (2013)
5. A.C. Bose, B. Balaya, P. Thangadurai, S. Ramasamy, J. Phys. Chem. Solids **64**, 659 (2003)
6. O.K. Varghese, L.K. Malhotra, G.L. Sharman, Sens. Actuators, B **55**, 161 (1999)
7. R.R. Kasar, N.G. Deshpande, Y.G. Gudage, J.C. Vyas, R. Sharma, Phys. B Phys. Cond. Matter **403**, 3724 (2008)
8. H.C. Chiru, C.S. Yeh, J. Phys. Chem. C **111**, 7256 (2007)
9. R. Khan, T.J. Kim, J. Hazard. Mater. **163**, 1179 (2009)
10. r Bhosale, S. Pujari, G. Muley, B. Pagare, A. Gambhire, J. Nanostructure Chem. **3**, 46 (2013)
11. R. Bargougui, A. Oueslati, G. Schmerber, C. Ulhaq-Bouillet, S. Colis, F. Hlel, S. Amma, A. Dinia, J. Mater. Sci. **25**, 2066 (2014)
12. W.A.N.G. Yan, F.A.N. Cai-mei, H.U.A. Bo, LIANG Zhen-hai, SUN Yan-pin. Trans. Nonferrous Met. Soc. China **19**, 778 (2009)
13. S.S. Roy, J. Podder Gilberto, J. Optoelect. Adv. Mater. **12**, 1479 (2010)
14. R.K. Nath, S.S. Nath, K. Sunar, J. Anal. Sci. Technol. **3**, 85 (2012)
15. M. Parthibavarman, V. Hariharan, C. Sekar, V.N. Singh, J. Optoelec. Adv. Mater. **12**, 1894 (2010)
16. K. Anandan, V. Rajendran, J. Phys. Sci. **19**, 129 (2014)
17. K. Vanheusden, W.L. Warren, C.H. Seager, D.R. Tallant, J.A. Voigt, B.E. Gnade, J. Appl. Phys. **79**, 7983 (1996)
18. T. Krishnakumar, R. Jayaprakash, M. Parthibavarman, A.R. Phani, V.N. Singh, B.R. Metha, Mater. Lett. **63**, 896 (2009)
19. A. Azam, A.S. Ahmed, S.S. Habib, A.H. Naqvi, J. Alloys Compd. **523**, 83 (2012)
20. S. Vadivel, G. Rajarajan, J. Mater. Sci. **26**, 3155 (2015)
21. K. Tennakone, J. Bandara, Appl. Catal. Part A. Gen. **208**, 335 (2001)
22. K. Vinodgopal, P.V. Kamat, Environ. Sci. Technol. **29**, 841 (1995)